Effect of multiple time delays on intensity fluctuation dynamics in fiber ring lasers

Anthony L. Franz,[1] Rajarshi Roy,[2,3,4] Leah B. Shaw,[5] and Ira B. Schwartz[6]
[1]*Department of Physics, United States Air Force Academy, Colorado Springs, Colorado 80840, USA*
[2]*Department of Physics, University of Maryland, College Park, Maryland 20742, USA*
[3]*IREAP, University of Maryland, College Park, Maryland 20742, USA*
[4]*IPST, University of Maryland, College Park, Maryland 20742, USA*
[5]*Department of Applied Science, College of William and Mary, Williamsburg, Virginia 23187, USA*
[6]*Nonlinear Systems Dynamics Section, Plasma Physics Division, Code 6792, U.S. Naval Research Laboratory, Washington, DC 20375, USA*

(Received 15 November 2007; revised manuscript received 11 March 2008; published 17 July 2008)

The effect of time delay on nonlinear oscillators is an important problem in the study of dynamical systems. The dynamics of an erbium-doped fiber ring laser with an extra loop providing time-delayed feedback is studied experimentally by measuring the intensity of the laser. The delay time for the feedback is varied from ~0.3 to ~900 times the cavity round-trip time, over four orders of magnitude, by changing the length of fiber in the delay line. Depending on the delay, we observe either regular oscillations or complex dynamics. The size of the fluctuations increases for delays long compared with the round-trip time of the laser cavity. The complexity of the fluctuations is quantified by creating spatiotemporal representations of the time series and performing a Karhunen-Loève decomposition. The complexity increases with increasing delay time. The experiment is extended by mutually coupling two fiber ring lasers together. The delay time for the mutual coupling is varied from ~0.2 to ~600 times the cavity round-trip time, over four orders of magnitude again. In this case the fluctuations are generally larger than the single laser case. The complexity of the dynamics for the mutually coupled system is less at short delays and larger at long delays when compared to the uncoupled case. The width of the optical spectra of the coupled lasers also narrows.

DOI: 10.1103/PhysRevE.78.016208 PACS number(s): 05.45.Tp, 42.65.Sf, 05.45.Xt, 42.55.Wd

I. INTRODUCTION

Many systems in nature and engineering interact with each other and communicate by way of some coupling mechanism. Since communicating signals between coupled systems have a finite velocity, there must be a nonzero finite delay in the coupling schemes. The dynamics of delay-coupled systems are rich and varied, and very important for the consideration of biological, chemical, and physical systems, including neurons, chemical reactions involving transport processes, laser systems, and electronic circuits [1,2]. Delays are often neglected for simplicity, and this may be a good approximation when they are very short compared to other system time scales. When this is not the case, as has become very clear over the past decade, time delays play a very important role in the dynamics and function of networks of coupled elements, and often influence their collective dynamics. Studies of single time-delayed systems show that increasing delays typically lead to more complex, high-dimensional dynamics [3]. The adaptive nature of systems with delays, such as the variability of the number of degrees of freedom involved at a given point in their time evolution, is of interest and significance for specific applications [4].

An excellent testbed for the examination of delayed coupling communication systems occurs in optical communication. Optical communication using chaotic wave forms offers potential advantages in terms of privacy [5] and robustness due to broadband transmission [6]. Recently, chaos-based communication was demonstrated over 120 km of commercial fiber optic line in Athens, Greece [6]. As chaotic communication systems and ideas are developed it will be important to understand how the components of the system interact over transmission lines that are kilometers long. Consequently, the dynamics of the coupled components in the presence of long delays needs to be understood. Previously optical communication using chaotic wave forms has been demonstrated in the laboratory with erbium-doped fiber ring lasers (EDFRL) [7,8]. Fiber lasers are attractive because of their high dimensionality and large bandwidth, which add to privacy [5], and offer the possibility of an all optical communication system [9].

A good understanding of the dynamics of EDFRLs is necessary to develop effective systems. The optical cavity of an EDFRL can be long enough that the round-trip time, τ_r, is hundreds of nanoseconds long and easily resolvable with modern detectors and oscilloscopes. Previous work [10] has taken advantage of the measurable resolution time and found that the light output has a steady-state intensity with small fluctuations about the mean. These fluctuations produce a pattern over one round trip that changes slowly over many subsequent round trips as noise modifies it [11]. The evolution of the patterns is very slow compared to τ_r. The patterns are not regular or periodic within the round trip, but are stable for hundreds of round trips.

Long cavity length and broad gain profile allow thousands of longitudinal modes to exist simultaneously in the cavity [11], preventing a reduction to a simple low-dimensional system, such as those used to model semiconductor lasers [12]. The lasers each have thousands of lasing modes that are nonlinear oscillators globally coupled through sharing population inversion. It is a daunting task to model the laser systems with hundreds or thousands of coupled-mode equations, since many unknown parameters relating to the mode-

coupling would be involved [13]. A time domain model that involves delay-differential equations has sometimes been employed as an alternative [2,11] but even this approach presents serious difficulties when long lengths of fiber with random birefringence fluctuations are involved. Because of these difficulties typical of fiber laser systems we chose to employ the Karhunen-Loève (KL) decomposition of spatiotemporal representations of the time series data. This process derives a data driven model of the system.

In communication systems, a single laser becomes useful when it interacts with other systems. Injection locking of lasers is a common practice that can be used to lock the frequency and phase of a laser to an injected signal if the injected signal is strong enough, as discussed in Chap. 9 of [14] and Sec. 7.3 of [15]. Previous modeling indicated that this can affect the intracavity dynamics of the laser [16]. Researchers have experimentally studied the synchronization of chaotic EDFRLs with unidirectional coupling where light is injected from one laser into a second laser [17–19]. These papers presented time series 1 ms long or greater and did not examine the intracavity dynamics. They also did not examine variations due to multiple coupling line lengths, and the coupling line lengths were short, except for the work of Kim *et al.* [19], which used a 1.5 km length coupling line. Mutual coupling of two EDFRLs can be achieved by injecting light from laser 1 into laser 2 and simultaneously injecting light from laser 2 into laser 1. The synchronization of mutually coupled chaotic lasers was recently studied experimentally and theoretically [20,21]. These papers examined the intracavity dynamics of the matched lasers with 46 m cavity lengths and used matched coupling lines 9 m long. The effect of coupling strength was analyzed in detail. When coupled with strong enough coupling, the two lasers became chaotic and delay synchronized with a delay equal to the length of the coupling lines. The intracavity intensity patterns repeated over several round trips. Another recent paper specifically analyzed the effect of the transmission line on the ability of a system to communicate using chaotic lasers [22]. This numerical work considered transmission lines hundreds of kilometers long, but only evaluated the quality of data transmission, not the effect of varying the transmission, or coupling, delay on the lasers' dynamics. There have also been many studies on leader-follower dynamics and switching in coupled semiconductor lasers [23].

A recent study examined the effect of time delays on the synchronization of semiconductor lasers using a cross correlation [24]. Their results showed that isochronal synchronization occurs for two mutually coupled lasers when the two lasers also have self-feedback. The time delays of the mutual coupling and self-feedback were equal. With self-feedback only, there was no synchronization because there was no mutual coupling. With mutual coupling only, achronal synchronization was observed and the cross-correlation peaks were offset from zero by the coupling delay time. As described in the next section, our work on fiber lasers examines the effects of feedback and mutual coupling separately.

II. OUTLINE

In this paper we experimentally analyze the effect of time-delayed input to EDRFLs to better understand the basic dynamics of the lasers when subjected to small delayed inputs. The EDFRLs are not forced to operate in a chaotic regime. We consider two basic configurations: (1) A single fiber ring laser with a self-feedback loop and (2) two fiber ring lasers that are mutually coupled with fiber delay lines. We consider a single fiber ring laser and add a feedback loop that we will add extra fiber to in order to vary the feedback delay time, τ. This delay is varied over four orders of magnitude to examine the effect of delay for cases where $\tau < \tau_r$, $\tau \approx \tau_r$, $\tau > \tau_r$, and $\tau \gg \tau_r$. We initially look at only a single laser with feedback for two reasons. First, EDFRL experiments use extra loops in the cavity to make communication more secure [7,19] and to generate multiple wavelengths [25]. Second, we want to have results from the simpler case of a single laser with feedback to compare to the results from the mutually coupled experiment. The coupling strength, κ, is monitored to keep it constant for all delays. We analyze the fluctuations using a variety of techniques to visualize and quantify the dynamical behavior observed. We also examine the optical spectra. These observations and analysis are repeated for two mutually coupled EDFRLs using coupling delays, also referred to as τ. Additionally, we examine the synchronization of the two EDFRLs.

We display the dynamics of the laser intensity using time-series plots, power spectra, time-delay embeddings, and a spatiotemporal representation of the time series. We use several methods to visualize different aspects of the dynamics. The time-series plots of the laser intensity show patterns in the dynamics such as regular oscillations and the round-trip repetition, or the apparent lack of regular structure. We will look at time series on the scale of both τ_r and τ. Power spectra show which frequencies dominate the dynamics. Time-delay embeddings are used to reconstruct the phase space of a dynamical system from a time series of experimental data [26,27]. Plots of the time series in these embeddings are a way to view the complexity of the time series and can illustrate the nature of the dynamical behavior. Finally, spatiotemporal representations are a way to visualize a time series that has dynamics with two different time scales in it [28]. The one-dimensional time series is recast into a two-dimensional (2D) representation by breaking the time series up into sections with a size determined by an important time scale. In previous work both the ring laser round-trip time [20,21] and the feedback delay time [28] have both been used. To build the spatiotemporal representation the time series is broken up into strips of data that are one time scale in length. These strips are then stacked on top of each other. The resulting data set is plotted with different colors representing different values of intensity, where each point is indexed by time within the time scale and the number of time scales. We used the round-trip time as our basis in order to compare the results for different delay times. The spatial part of the representation comes from mapping the times within a round trip to positions along the ring cavity [29]. This idea uses Taylor's hypothesis from fluid mechanics [30], which states that if a fluid flow is fast enough a spatial pattern of turbulence can be measured by a single detector at a fixed location as the fluid moves past it. In our case the light propagating around the ring is the flow and the relatively stable round-trip patterns are measured at a single point at

the output of the ring cavity. These plots can display large amounts of data compactly and show features with different time scales so that the round-trip pattern stability can be observed and comparisons made between data sets. These four methods provide different ways of visualizing data that give us a qualitative understanding of the dynamics. We use them as a starting point to derive quantitative measures of the dynamical characteristics.

The size of the fluctuations in a time series is quantified by the ratio of the standard deviation of the time series to its mean. Normalizing to the mean allows us to compare the relative fluctuation size between data sets. To quantify the complexity of the dynamics we perform a KL decomposition on the spatiotemporal representation [31]. KL decomposition has many other names, including proper orthogonal decomposition and principal component analysis [32]. Previous work with lasers has used this technique to analyze numerical and experimental data sets of one-dimensional spatial patterns of intensity from multiple stripe and broad area semiconductor lasers [33]. Here, we apply the technique to the data in our spatiotemporal representation. This data has the same format as the data in the previous work cited, but we form our spatial dimension from our map to ring position in the spatiotemporal representation. We consider two methods to quantify the complexity using the results of the KL decomposition. First, we note that the number of KL modes needed to reconstruct the system dynamics to a given accuracy will be small for round-trip patterns that are consistently present in the dynamics and larger when the dynamics are composed of many different patterns over the time scale considered. This gives us a measure of the overall complexity of the time series. Second, we interpret the eigenvalues of the KL modes to be the probabilities that the mode will occur [31,34] and calculate the Shannon entropy, or information, of the modes [35].

The variation of the widths and heights of peaks in the optical spectra are also considered to determine if the lasing wavelength is affected by the second feedback loop or coupling to a second laser. Spectral measurements provide us with a means to assess the influence of the feedback or coupling on the coherence properties of the lasers.

III. RING LASER WITH FEEDBACK

Figure 1 shows the setup for the experiment with feedback. The laser has an erbium-doped fiber amplifier and is tuned to operate at a wavelength of 1550 nm using the polarization controller. The laser was pumped at 8.0 times the threshold pumping rate. Fiber couplers are used to guide light out of one fiber and inject it into another fiber. Optical isolators enforce the propagation direction around the ring. Some of the light is routed from the ring through a feedback line into which different lengths of fiber are inserted to change the delay time of the feedback.

We measured the round-trip time of the ring by making use of the repetition of the round-trip patterns. This repetition occurs because the upper laser level lifetime is very long (≈ 10 μs) so the population inversion responds very slowly compared to the laser field. We calculate the power spectra of

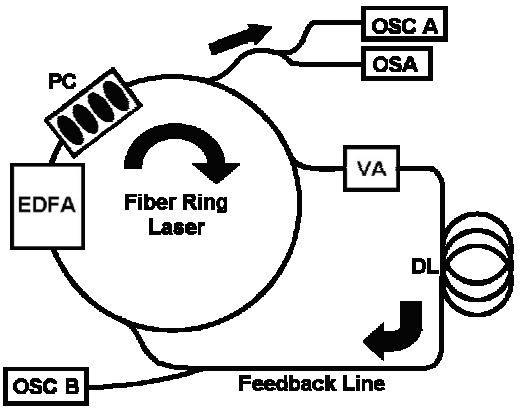

FIG. 1. Experimental setup for the laser with feedback. The arrows show the direction of light propagation through the ring and the feedback line. EDFA, erbium-doped fiber amplifier; PC, polarization controller consisting of a sequence of linear polarizer, one-quarter wave plate, one-half wave plate, and one-quarter wave plate; VA, variable attenuator; DL, delay line; OSC A, photodetector and oscilloscope used to measure laser dynamics; OSC B, photodetector and oscilloscope used to monitor the feedback line; OSA, optical spectrum analyzer.

five 1-ms time series of intensity data. Because of the round-trip repetition there is a spectral peak at the round-trip time along with higher harmonics. We average the frequency of the first peak for all five spectra and invert it to find $\tau_r = 213.9$ ns, which corresponds to a cavity length of about 44 m.

The feedback line length varied from 14 m to 38 km which corresponds to delay times of 0.068 μs to 187 μs. This wide range of times allows us to see how the dynamics are affected when τ is less than, comparable to, and larger than τ_r. The light intensity in the feedback line is monitored with an oscilloscope. A variable attenuator is used to adjust the light levels in the line. This allows us to correct for the different losses in the different lengths of the feedback line and to keep the coupling strength constant for all of the data runs. The coupling strength is defined as the ratio of the power injected into the ring from the feedback line to the power in the ring. In the experiments described here we chose $\kappa = 1\%$. This coupling strength was set by the losses in the couplers and connectors and the amount of absorption in the 38 km line. We used the variable attenuator to keep κ constant. The light intensity is measured by a 125 MHz bandwidth photodetector and a digital oscilloscope sampling every 1.0 ns. Five 1-ms-long time series are recorded for each delay time. An optical spectrum analyzer is used to monitor the wavelength of the laser.

A. Fluctuation size and dynamical complexity of round-trip patterns

We normalize the intensity time series by dividing each one by its mean. The means of the intensities remained constant. The dynamics of the normalized laser output is plotted over five round trips in Fig. 2(a) for the laser without feedback. Figures 2(b)–2(i) show the results for the laser with

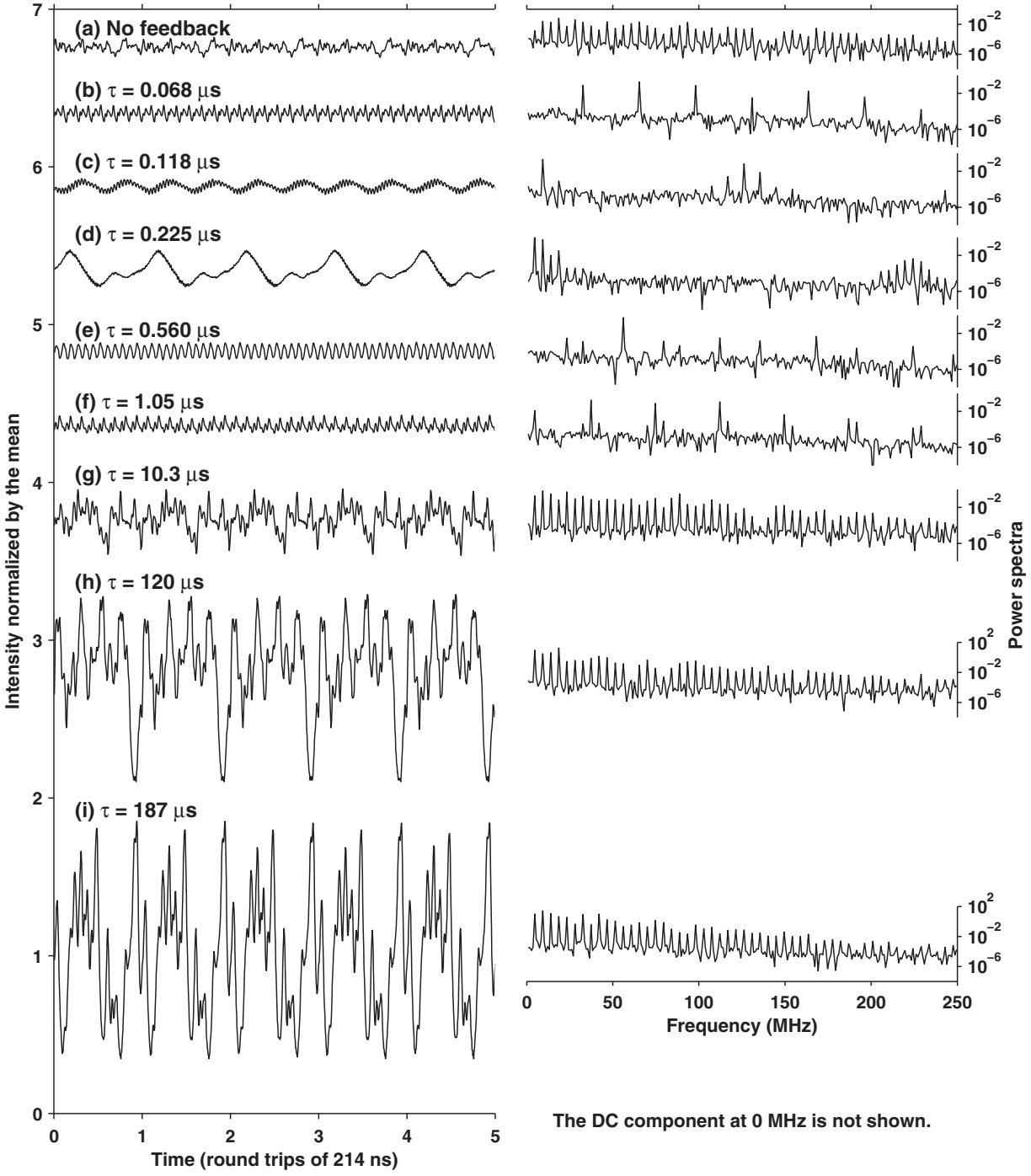

FIG. 2. The left-hand column shows laser output intensities over five round trips where the round-trip time is 214 ns. Each time series is normalized by its mean, and the plots are offset for clarity. (a) is for the laser without feedback. (b)–(i) are for the laser with feedback with the time delay, τ, given. The right-hand column has power spectra of the five round trips shown for each time series. The DC component at 0 Hz has been omitted to better show the detail of the spectra.

feedback with various delays. The plots in the figure have been offset for clarity. Without the offset they would all be centered on an intensity of 1 due to the normalization. Periodic dynamics is usually observed at a delay time τ of 1 μs or less, with periods much smaller than τ_r. Figures 2(c) and 2(d) display patterns with a period of approximately one-half the round-trip time and one round trip, respectively. The last three plots show that the dynamics repeat over a round trip, that the magnitude of the fluctuations increases for large delays, and that the patterns within a round trip are very irregular compared to the regular oscillations at shorter delays. Note that the intensity scale is the same for all plots, so the relative increase in intensity fluctuations is conspicuous. The power spectra of the five round-trip time series are shown in the right-hand column of Fig. 2. The dc component at 0 MHz was omitted for clarity. The spectrum for the case without feedback [plot (a)] has harmonics of the round-trip time. Plots (b)–(f) have spectra with specific peaks that are indica-

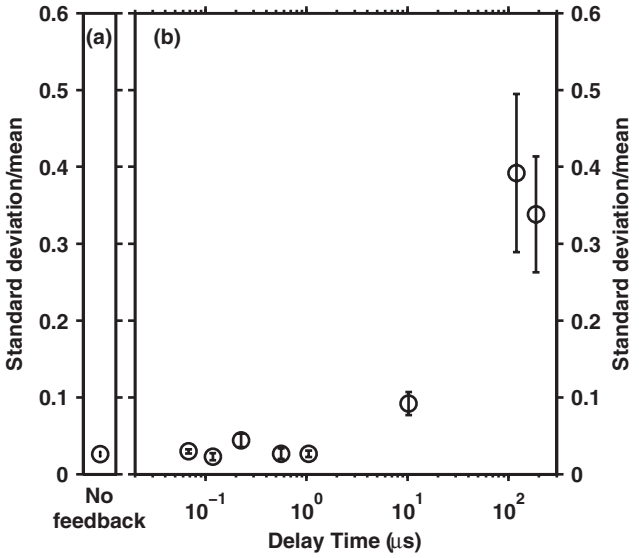

FIG. 3. (a) Ratio of standard deviation to the mean for the laser without feedback. (b) Ratio of standard deviation to the mean for the laser with feedback of different delays. The error bars in both plots are the statistical standard error based on a sample set of five.

tive of periodic dynamics. Plots (g)–(i) again show harmonics of the round-trip time and a rising background level as the dynamics become more complicated. Here we see that the dynamics are qualitatively changing as we adjust the delay time. At short delays the time series are periodic and can be represented by a few Fourier modes while many more modes are required at longer delays.

To quantify the increase in fluctuation size seen in the time-series plots, we examine the variation of the means and standard deviations of the time series with varying feedback delay time. The means remain approximately constant over the changing delay, but the standard deviations increase. To compare the increase we calculate the ratio of the standard deviation of the time series to its mean. Figure 3 shows the mean and standard error of these ratios for the five time series taken at each delay. The standard deviation increases from 3% of the mean for the laser without feedback and shorter delay times to around 35% of the mean at long delays. To interpret these results, we should note that the feedback level has been carefully maintained constant at $\kappa=1\%$. The dramatic rise in the standard deviation is seen to occur at the 10 μs delay. The large error bars on the last two data points are caused by the changing temporal patterns for the intensity time series that were sampled to compute the standard deviation. These statistics describe the size of the fluctuations but do not tell us about the complexity and variability of the round-trip patterns.

Another way to visualize the data to help us see the complexity of a round-trip pattern is with a time-delay embedding. These are usually used to reconstruct the phase space of a dynamical system and require careful calculation of the number of dimensions needed to unfold the attractor and the proper delays to use to sample the data [26,27]. Because the goal of our embeddings is merely to obtain a qualitative sense of the complexity of a round-trip pattern, we use only three dimensions and do not calculate the number of dimensions needed to thoroughly represent the phase space. The resulting trajectories are projections into three dimensions of the true phase-space trajectories. Each point of the trajectory has three coordinates: $I(t-T_1-T_2)$, $I(t-T_1)$, and $I(t)$ where $I(t)$ is the intensity at time t and T_1 and T_2 are the embedding delays. Following the procedure recommended in Ref. [36] the first minimum of the mutual information of the time series is used to determine the embedding delay. The average mutual information (in bits) between time series X and time series Y, $M(Y;X)$ is

$$M(Y;X)=\sum_{x,y}p(x,y)\log_2\left(\frac{p(x,y)}{p(x)p(y)}\right), \tag{1}$$

where $p(x,y)$ is the joint probability that $X=x$ and $Y=y$, and $p(x)$ and $p(y)$ are the marginal probabilities that $X=x$ and $Y=y$, respectively. In our case, $X\rightarrow I(t)$ and $Y\rightarrow I(t-T_1)$. The mutual information gives the reduction in the uncertainty of Y for a given measurement of X [35]. The longer the delay, the more the coordinates will become uncorrelated. Using the first minimum gives us the most independent pair of coordinates that are not completely uncorrelated. To find the second embedding delay, T_2, we use the minimum of the mutual information of Z given X and Y [37]. We calculate the second delay using the minimum of the mutual information

$$M(Z;X,Y)=\sum_{x,y,z}p(x,y,z)\log_2\left(\frac{p(x,y,z)}{p(x,y)p(z)}\right), \tag{2}$$

where $p(x,y,z)$ is the joint probability that $X=x$, $Y=y$, and $Z=z$. For both Eqs. (1) and (2) the probabilities are calculated using histograms of the entire 1-ms time series with 25 bins for each dimension. The intensities of each time series are rescaled from 0 to 1 and the histogram applied over this range. The embedding delays calculated are used to qualitatively examine the complexity of a typical round-trip pattern for each feedback delay case.

Figure 4 shows the time-delay embedding of the first round trip shown in each of the plots in Fig. 2. Comparing plot (a) for the laser without feedback to plots (b)–(f) shows that feedback with a short delay simplifies the round-trip patterns. The cloud in plot (a) is transformed into more organized structures of loops. The high-frequency features in Figs. 2(c) and 2(d) appear in Figs. 4(c) and 4(d) as small oscillations overlaid on the low-frequency structures. In plot (g) where the time delay is increased to 10.3 μs, the round-trip patterns become complex again and are qualitatively similar to plot (a), but with larger fluctuations. At long delays the fluctuation size increases dramatically, and so plots (h) and (i) require a larger scale to display the data. These two plots also show that the round-trip structure is more complex at long delays than at short delays. The time-delay embeddings provide a qualitative view of the complexity of a round trip. Now we proceed to examine the long-term evolution of the round-trip patterns over the entire time series.

B. Spatiotemporal representation

To examine the complexity and variability of the round-trip patterns, the time series must be represented in a new

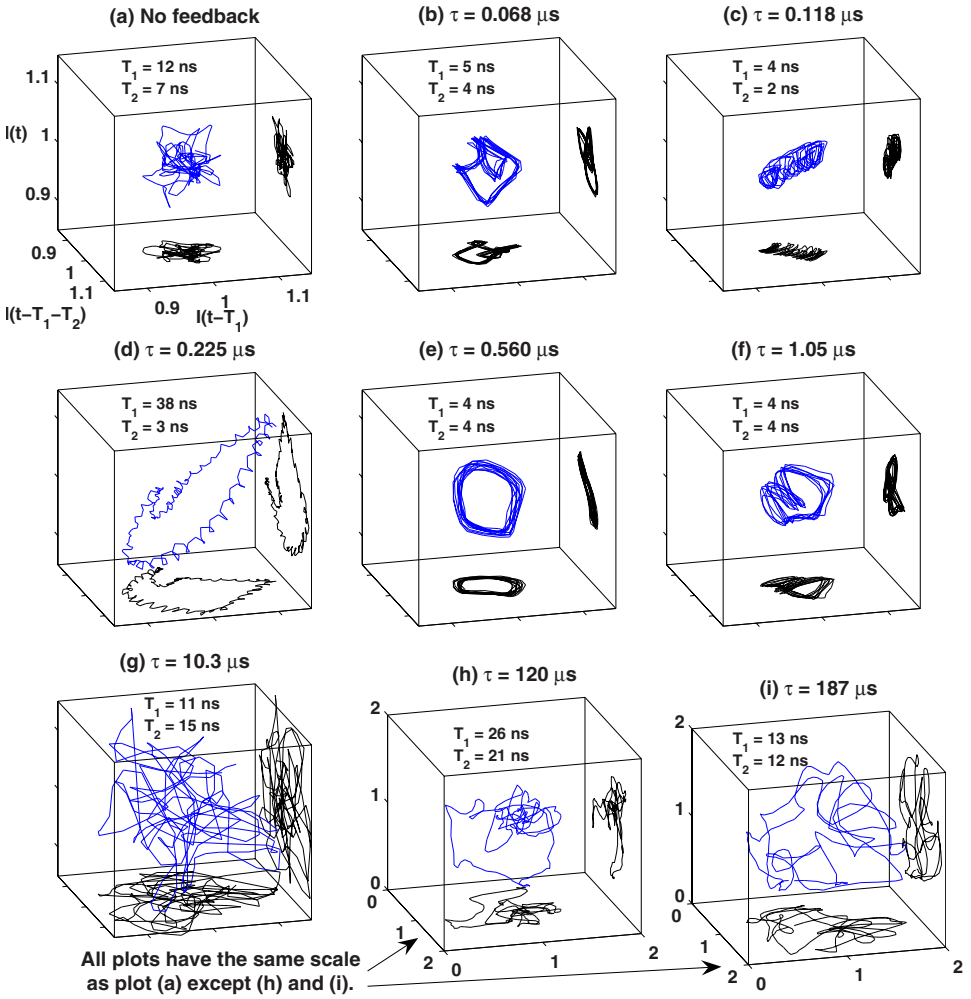

FIG. 4. (Color online) Time-delay embeddings of the first round trip shown in Fig. 2. Plot (a) is for the laser without feedback. The rest of the plots are for the laser with feedback with the time delay, τ, given. The embedding delays, T_1 and T_2, are also given. The gray (blue) curve is the three-dimensional trajectory, and the black curves are 2D projections onto the bottom and right-hand sides of the plots. The data points are 1 ns apart. Plots (a)–(g) have the same scale. Plots (h) and (i) have a larger scale due to the larger fluctuations in these time series. The plots are centered about 1 because each time series was normalized to its mean.

way that shows us information on the time scales of τ_r and τ. A spatiotemporal representation of the data is used to examine the dynamics of a system over many intervals of τ_r. We use τ_r since τ varies from run to run and τ_r is consistent for all of the time series.

To reduce the amount of data to more manageable sizes, we plot only every tenth round trip of 4500 total round trips. Since the round-trip patterns do not change over the scale of 10 round trips, we still obtain an accurate representation of the dynamics (Fig. 2 shows this stability over five round trips). Each time series is rescaled from 0 to 1 to better see the features in the fluctuations. Now two problems must be addressed to create the spatiotemporal representations. First, the time series is composed of discrete data, and the end of the round trip will most likely lie in the gap between measurements. We improve our precision in this respect by linearly interpolating nine data points between our existing data to give a resolution of 0.1 ns. The second issue is that there is uncertainty in the round-trip time measurement, so we do not know exactly which data point to use to start the next round trip. This error grows as we skip round trips. We can sidestep this problem by using the fact that the intensity pattern repeats every round trip. To determine the starting element of the next round trip to stack on our plot, we use a correlation measure

$$C(s) = \sum_i [I_{n-1}(t_i) - \langle I_{n-1}\rangle][I_n(t_i + s) - \langle I_{n,s}\rangle], \qquad (3)$$

where $I_{n-1}(t_i)$ is the intensity of the previous round trip where t_i indexes the position in the ring, $I_n(t_i)$ is the intensity of the current round trip at position t_i, $\langle I_{n-1}\rangle$ is the time average over the previous round trip, and $\langle I_{n,s}\rangle$ is the time average of the current round trip shifted by s [38]. A range of ± 5 ns centered on the estimate of the starting point was used for s. The correlation usually selected elements within a range of ± 1 ns or less of the estimate. The correlation will favor lining up high-frequency structures more than low-frequency structures because the high-frequency structures vary more over the correlation range. Low-frequency components do not vary much over a small range, and so the correlation from a low-frequency signal is more uniform, allowing noise or other features more influence on $C(s)$. A tighter range on s of ± 1 ns was needed for the case where τ=219 ns because these time series had a significant low-frequency component with a small amplitude high-frequency component overlaid on it. The larger range of s allowed the correlation to select starting points that were far apart from each other, resulting in artificial discontinuities.

Figure 5 shows spatiotemporal representations for the first 4500 round trips (using every tenth round trip) of the time

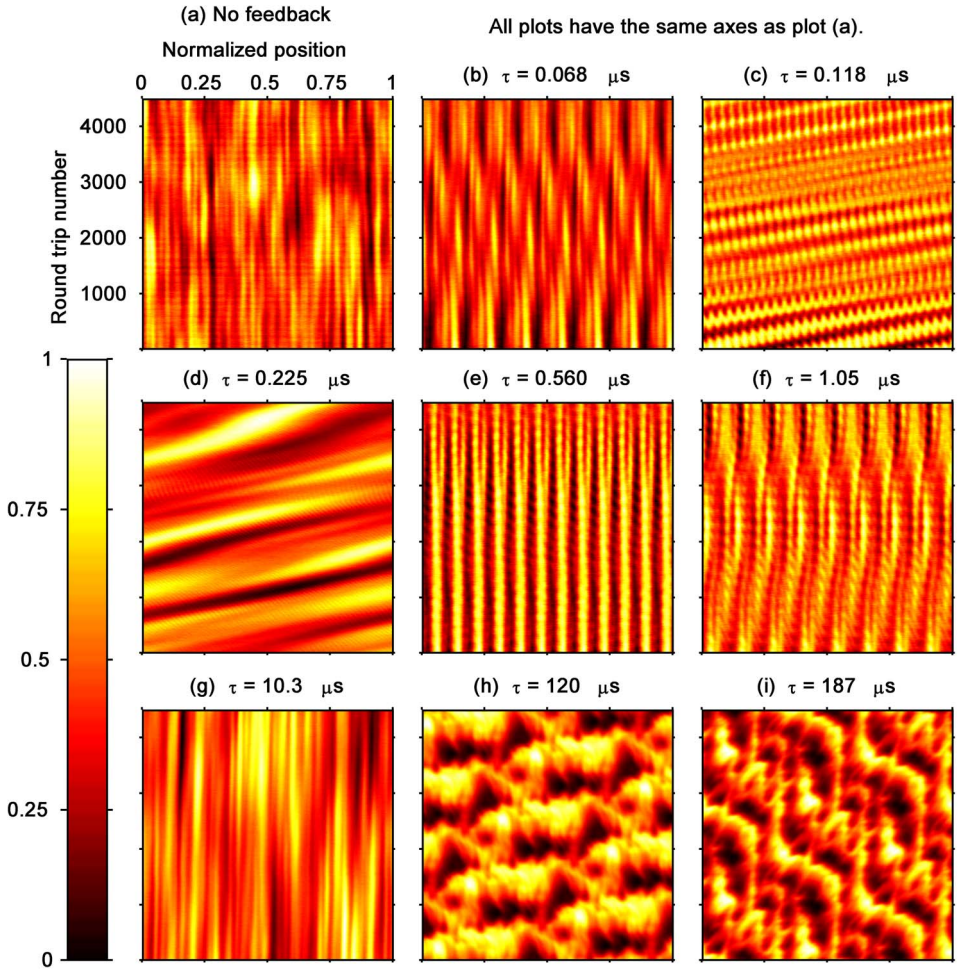

FIG. 5. (Color online) Spatiotemporal representations of the intensity dynamics for a laser with (a) no feedback and (b)–(i) feedback with the time delay, τ, listed. The laser intensities are rescaled from 0 to 1 for each time series, with the color bar indicating the value of the normalized intensity on the plots. All plots have the same axes as plot (a). Every tenth round trip is plotted.

series plotted in Fig. 2 and Fig. 4. The data shown in the previous figures occurs around round trip 2340 in the plots of Fig. 5. The variety of dynamics produced when changing the feedback delay time is illustrated clearly. Figure 5(a) shows the dynamics of the laser without feedback. More information can be presented in this type of plot than in a time-series plot. Structures in the round-trip pattern can be stable for hundreds or even 1000 round trips or may slowly vary on these time scales. There is little regular structure within a round trip. Figures 5(b), 5(e), and 5(f) show patterns of vertical stripes. These stripes correspond to the regular oscillations seen in Fig. 2 for these cases. The round-trip patterns can be stable for hundreds of round trips, and certain oscillation frequencies are maintained even as the patterns evolve into new periodic patterns. Figure 2(c) shows a high-frequency oscillation overlaid on a low-frequency oscillation. The corresponding power spectrum shows a peak at 2 times the round-trip frequency and group of three peaks near 125 MHz. Figure 5(c) shows us that the low-frequency oscillation is not a harmonic of the round-trip frequency. The low-frequency peaks travel along the ring while the high-frequency peaks stay in place. The same phenomenon occurs in Fig. 5(d), but it is hard to see the high-frequency oscillation because it has a small amplitude. It is visible in the power spectrum as a collection of peaks near 225 MHz and can also be seen in the time-delay embedding in Fig. 4(d). Analysis of the power spectra for these two cases shows that the high-frequency oscillations are harmonics of the frequency corresponding to a period of 213.95 ns, and the low-frequency oscillations are harmonics of the frequency corresponding to 214.22 ns. This could be caused by two polarization states that oscillate in the cavity simultaneously at different wavelengths due to the birefringence in the fiber. Figure 5(g) shows that the regularity of the round-trip pattern is lost for longer delays. Figures 5(h) and 5(i) show how the character of the plot changes for the longest time delays. Closer examination reveals that two-dimensional features repeat themselves with a period equal to the feedback delay. While looking at the data on the scale of a round trip shows a complex pattern, the spatiotemporal representation shows that these patterns quickly vanish but reappear hundreds or even 1000 round trips later. The spatial position of the patterns shifts because τ is not commensurate with τ_r. The time scale of the delayed feedback is being imprinted on the dynamics.

The long τ time series show repetition of a pattern with a period of τ. Figure 6 shows the full 1-ms time series from which the data in Figs. 5(h) and 5(i) was extracted. The case for the laser without feedback is shown for comparison, and bars of length τ are shown on the plots for the cases with feedback. The spatiotemporal representations in Fig. 5(h) and 5(i) show that these long time-scale patterns have com-

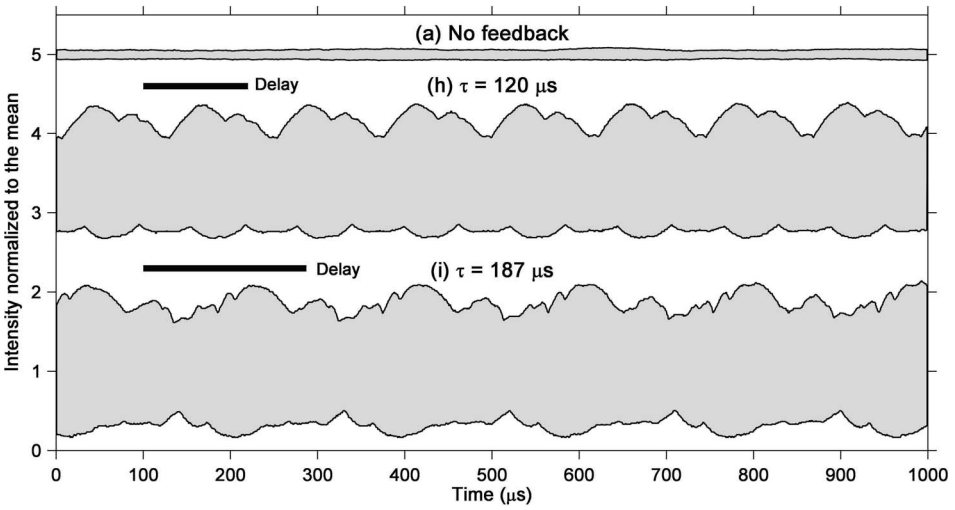

FIG. 6. Envelope of the full 1-ms time series of the intensity dynamics for a laser with (a) no feedback and (h)–(i) feedback with the time delay, τ, listed. The labeling corresponds to the plots in previous figures. (a) and (h) are offset for clarity. The bars on plots (h) and (i) visually show the length of τ for each plot.

plex round-trip patterns. These round-trip patterns evolve and reappear over 100 μs later as the overall pattern repeats every τ. The long pattern is essentially stored in the long transmission lines in the characteristics of the light moving through the lines. As the signal is fed into the second laser cavity, it is "processed" to reproduce the intensity pattern.

C. Karhunen-Loève decomposition and spatiotemporal complexity

The complexity of the dynamics can be quantified by taking KL decompositions of the spatiotemporal representations. The procedure [31,38–40] is performed on a set of spatiotemporal data $u(x_j,n_t)$ which is a discrete array of data with each point indexed by a position around the ring, x_j, and a round-trip number, n_t. First, for each value of x_j we subtract the mean for that position j averaged over all n_t. Next, we compute the autocorrelation matrix, **K**, with elements

$$K(x_j,x_{j'}) = \langle u(x_j,n_t)u(x_{j'},n_t)\rangle, \tag{4}$$

where the angle brackets refer to time averaging. Then we calculate the eigenvalues $\tilde{\lambda}_i$ and eigenvectors ψ_i of **K**. The eigenvectors are orthogonal KL modes that describe a spatial pattern of the intensity over a round trip. The original data can be written in terms of an expansion

$$u(x_j,n_t) = \sum_i \alpha_i(n_t)\psi_i(x_j) \tag{5}$$

that uses the KL modes, $\psi_i(x_j)$, as its basis. Each mode has a coefficient, $\alpha_i(n_t)$, that weights the impact of that mode on the round-trip pattern at round trip n_t. The coefficients as a function of time are calculated with $\alpha_i(n_t)=\Sigma_j u(x_j,n_t)\psi_i(x_j)$, where

$$\langle \alpha_i(n_t)\alpha_k(n_t)\rangle = \tilde{\lambda}_i\delta_{ik}. \tag{6}$$

$\tilde{\lambda}_i$ is the eigenvalue corresponding to KL mode i and δ_{ik} is the Kronecker δ function. The coefficients come from projections of the data onto the KL modes, so the larger the eigenvalue the more the KL mode represents the structure of the round-trip pattern. The modes with the largest eigenvalues will be the most important in the expansion of Eq. (5) so we order the eigenvalues from largest, $\tilde{\lambda}_1$, to smallest, $\tilde{\lambda}_n$, and normalize them by the sum of all the eigenvalues. These normalized eigenvalues, λ_i, will be used to determine the complexity of the data.

Figure 7 shows the results of a KL decomposition on the spatiotemporal representation in Fig. 5(g) with a time delay of 10.3 μs. Figure 7(a) is the spatiotemporal representation. Figure 7(b) shows the three KL modes where mode 1 has the largest eigenvalue, mode 2 has the second largest eigenvalue, and so on. Mode 1 dominates early and again at the end of the data after its coefficient, plotted in Fig. 7(c), changes sign half-way through. Mode 2 is significant for most round trips and mode 10 has very little impact on the dynamics at any time. An example of a KL decomposition on a more complex time series is shown in Fig. 17 below.

The first method of quantifying the complexity considers how many terms are needed in the expansion in Eq. (5) to accurately reconstruct the original spatiotemporal data set [31,40–42]. This number has been called the KL dimension, D_{KL}, in previous work [42]. The importance of the mode to the reconstruction is given by the eigenvalues, λ, through the relation in Eq. (6). Figure 7(d) shows a logarithmic plot of the eigenvalue spectrum for the 25 largest eigenvalues on the left-hand (red) vertical axis. The rate of decay is very large for smaller i and then levels off at a smaller decay rate after about $i=12$. The eigenvalues decay more quickly than exponentially at first, meaning that the expansion in Eq. (5) can represent the spatiotemporal data accurately with only a few terms. Data with stable structures can be represented by a few KL modes, but changing round-trip patterns will require more KL modes to describe the evolving structures. To determine how many modes, D_{KL}, are needed, we sort the normalized eigenvalues in decreasing order and compute

$$S(N) = \sum_{i=1}^{N} \lambda_i \tag{7}$$

until $S(N)\geq 0.95$, where $i=1$ corresponds to the largest eigenvalue, $i=2$ corresponds to the second largest eigenvalue, and so on. The smallest value of N that meets the criteria is

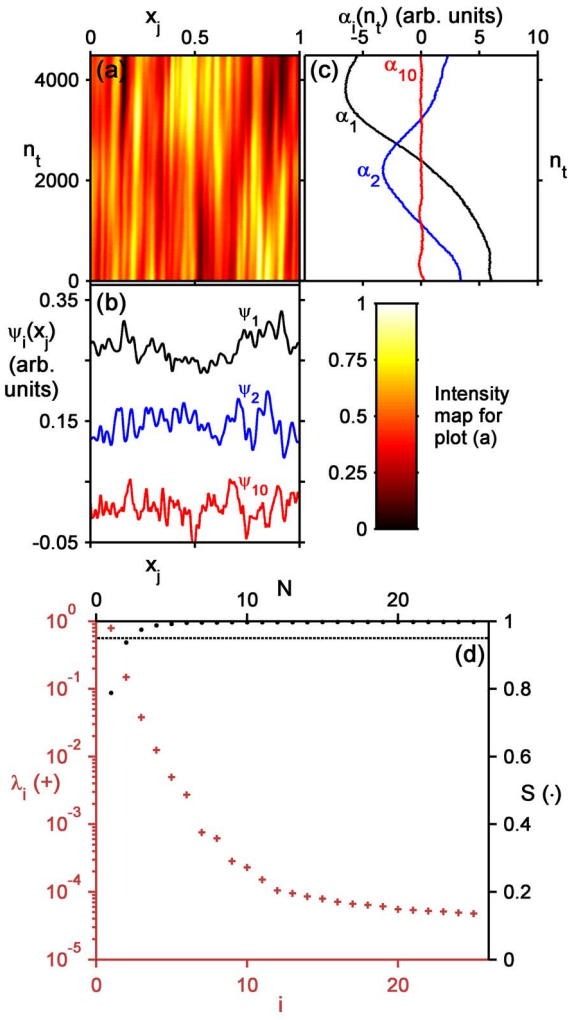

FIG. 7. (Color online) KL decomposition for $\tau=10.3$ μs. (a) Spatiotemporal representation of the intensity dynamics from Fig. 5(g). (b) KL modes associated with the largest two eigenvalues and the tenth largest eigenvalue. Modes 1 and 2 are offset for clarity. (c) Expansion coefficients for the KL modes in (b). (d) The 25 largest eigenvalues are plotted on the left-hand axis with gray +'s (red +'s), and the cumulative sum of the eigenvalues is plotted with black dots on the right-hand axis. The eigenvalues are normalized by the sum of all the eigenvalues. The dotted line shows the cutoff $S=0.95$.

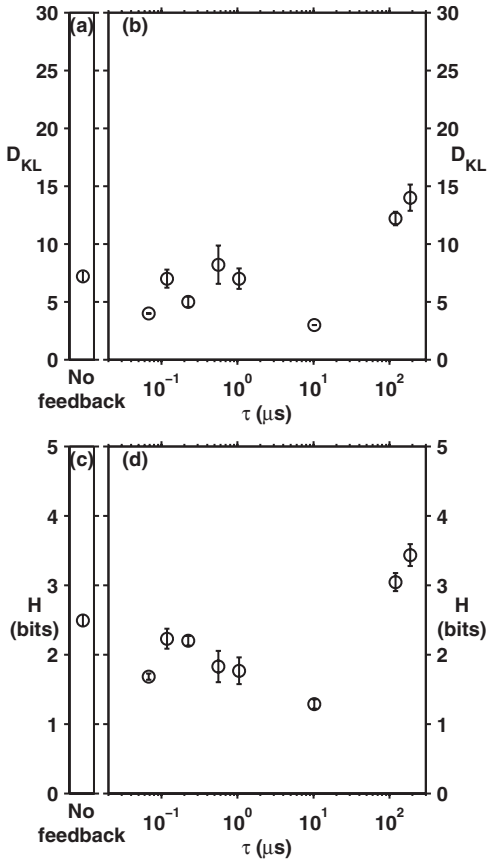

FIG. 8. (a) Number of KL modes needed to reconstruct the spatiotemporal plot for the laser without feedback to 95% accuracy. (b) Number of KL modes needed for 95% accurate reconstruction of the spatiotemporal plot for the laser with feedback of different delays. (c) Entropy for the laser without feedback. (d) Entropy for the laser coupled with feedback of different delays. The error bars in these plots are the statistical standard error based on a sample set of five.

the value assigned to D_{KL}. The 95% level was chosen arbitrarily. Figure 7(d) shows $S(N)$ and the 95% cutoff. For this case three modes are needed to achieve a 95% reconstruction accuracy using Eq. (5). Figure 8(a) shows the average number of KL modes for the laser without feedback needed to represent the intensity wave forms with 95% accuracy. Figure 8(b) is the same but for the laser with different feedback delays. The number of modes needed for accurate representation increases for larger delays as the delay time scale impresses itself on the dynamics, the round-trip patterns vary more from round trip to round trip, and the overall dynamics becomes more complex.

This method suffers from the arbitrary 95% accuracy requirement and the difficulty in selecting this value when the eigenvalue distributions have a knee in them such as the one around $i=12$ in Fig. 7(d). The second method uses the entire eigenvalue spectra through a connection with information theory. We interpret λ_i to be probability to find the system in the state ψ_i [31,34] and calculate the entropy H,

$$H=-\sum_i P_i \log_2 P_i=-\sum_i \lambda_i \log_2 \lambda_i. \tag{8}$$

This measure of complexity considers the KL modes to be states of the system. If only one KL mode described the system ($\lambda_1=1,\lambda_{i\neq 1}=0$) then $H=0$ because our uncertainty about the state of the system would be zero. Additionally, it has been proven that the KL basis minimizes the Shannon entropy as calculated with Eq. (8) [31,34].

We calculated H for several 2D images of uniformly distributed random numbers with the same number of pixels as our spatiotemporal representations. These images had an average value of H of about 8 bits per pixel [43]. Figure 8(c) shows the Shannon entropy for the laser without feedback and Fig. 8(d) shows the entropy for the laser with delayed feedback. The Shannon entropy decreases from 2.5 for the laser without feedback to a minimum of about 1.3 for the

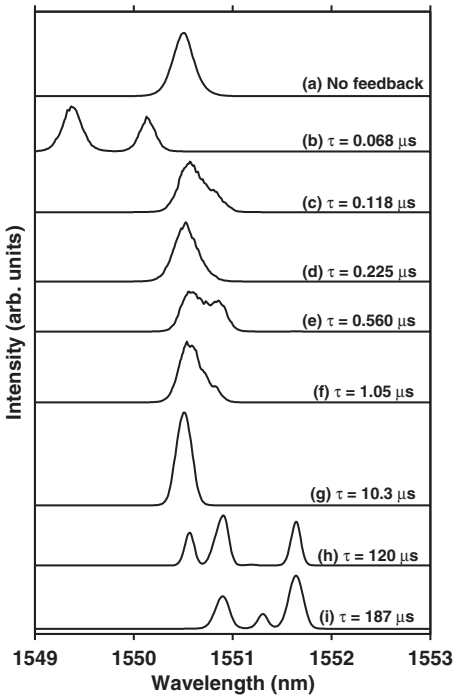

FIG. 9. Optical spectra of the laser. (a) is for the laser without feedback. (b)–(i) are for a laser with feedback with a delay, τ, as listed.

laser with feedback delayed by 10 μs. The Shannon entropy went up for the longest two delays to around 3. These results are similar to the results from calculating D_{KL} in the first method except here we see a decrease in complexity for short delays that was not observed in Fig. 8(b).

D. Optical spectra

The optical spectra of the laser are presented in Fig. 9. The optical spectrum analyzer data acquisition is not fast enough to capture the optical spectra on the time scale of a round trip. Each peak is a spectral envelope of the wavelengths measured over the scan time. Due to the length of the laser cavity, there are thousands of cavity modes that fit within the envelopes. The resolution of the spectrum analyzer is 0.1 nm. When feedback is applied, we often notice the presence of additional peaks, and the lasing frequency is generally spread over a wider wavelength range than for the laser without feedback. When the spectral peaks are separated we can usually observe that the width of the peaks are comparable to case (a) without feedback.

IV. TWO MUTUALLY COUPLED RING LASERS

We now want to compare the measurements for a single laser with feedback with what is observed when two fiber lasers are mutually coupled together with a delay, τ. We repeat the measurements and analysis of the preceding section with two coupled ring lasers whose cavity lengths are within 1 cm of each other and have τ_r=213.9 ns. The active fiber in the two amplifiers is identically doped and matched in length to within 1 mm. The experimental setup is shown in Fig. 10.

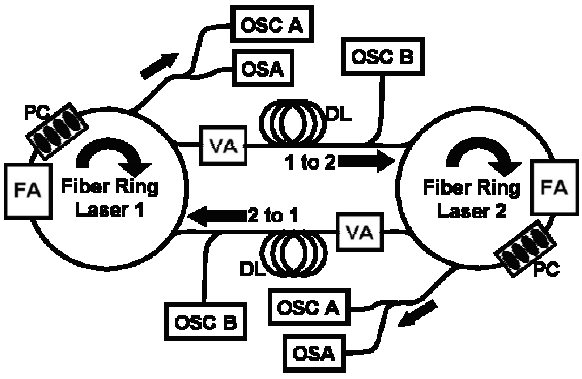

FIG. 10. Experimental setup for two coupled lasers. The arrows show the direction of light propagation through the rings and the coupling lines. FA, erbium-doped fiber amplifier; PC, polarization controller; VA, variable attenuator; DL, delay line; OSC A, photodetector and oscilloscope used to measure laser dynamics; OSC B, photodetector and oscilloscope used to monitor the coupling lines; OSA, optical spectrum analyzer.

The power in both rings was matched by adjusting the pumps, and the variable attenuators were used to match the power in the coupling lines. Laser 1 was pumped at 4.7 times its threshold pumping level, and laser 2 was pumped at 4.6 times its threshold. The coupling strength, κ, was 1.7% for this setup. Extra fiber was added to the coupling lines to vary the coupling time, τ, from 0.050 μs to 120 μs. Ten time series were taken for each delay time.

A. Fluctuation size and dynamical complexity of round-trip patterns

The dynamics of the normalized laser output is plotted over five round trips in Fig. 11(a) for the uncoupled lasers. The time series for laser 1 is offset above laser 2 for all plots in Fig. 11. The time-series pairs are also offset for clarity since their means all lie at 1 due to the normalization. Figures 11(b)–11(h) show the results for the mutually coupled lasers with the delays listed. The power spectra of the five round trips for laser 1 is shown in the left-hand column. Like the single laser with feedback, the coupled laser system shows a variety of dynamics starting with regular patterns in (b)–(f). A superposition of patterns with high and low frequencies is seen in (e), making a transition to complicated patterns repeating every round trip in (g) and (h). The size of the fluctuations increases for the coupled lasers even at the shortest delays. The power spectra show that the uncoupled lasers require many Fourier modes to represent them, but that the dynamics for short delays are very periodic and require only a few Fourier modes. For long delays the dynamics become more complicated and the background level of the power spectra rise. We see again a shift in the dynamics from simple to complex as the delay increases.

To quantify the increase in fluctuation size we plot the ratio of the standard deviation to the mean as before. Figure 12 shows the ratios for the mutually coupled lasers and also includes the data from Fig. 3 for comparison. In plot (a) there are two values for laser 1 because two sets of data were

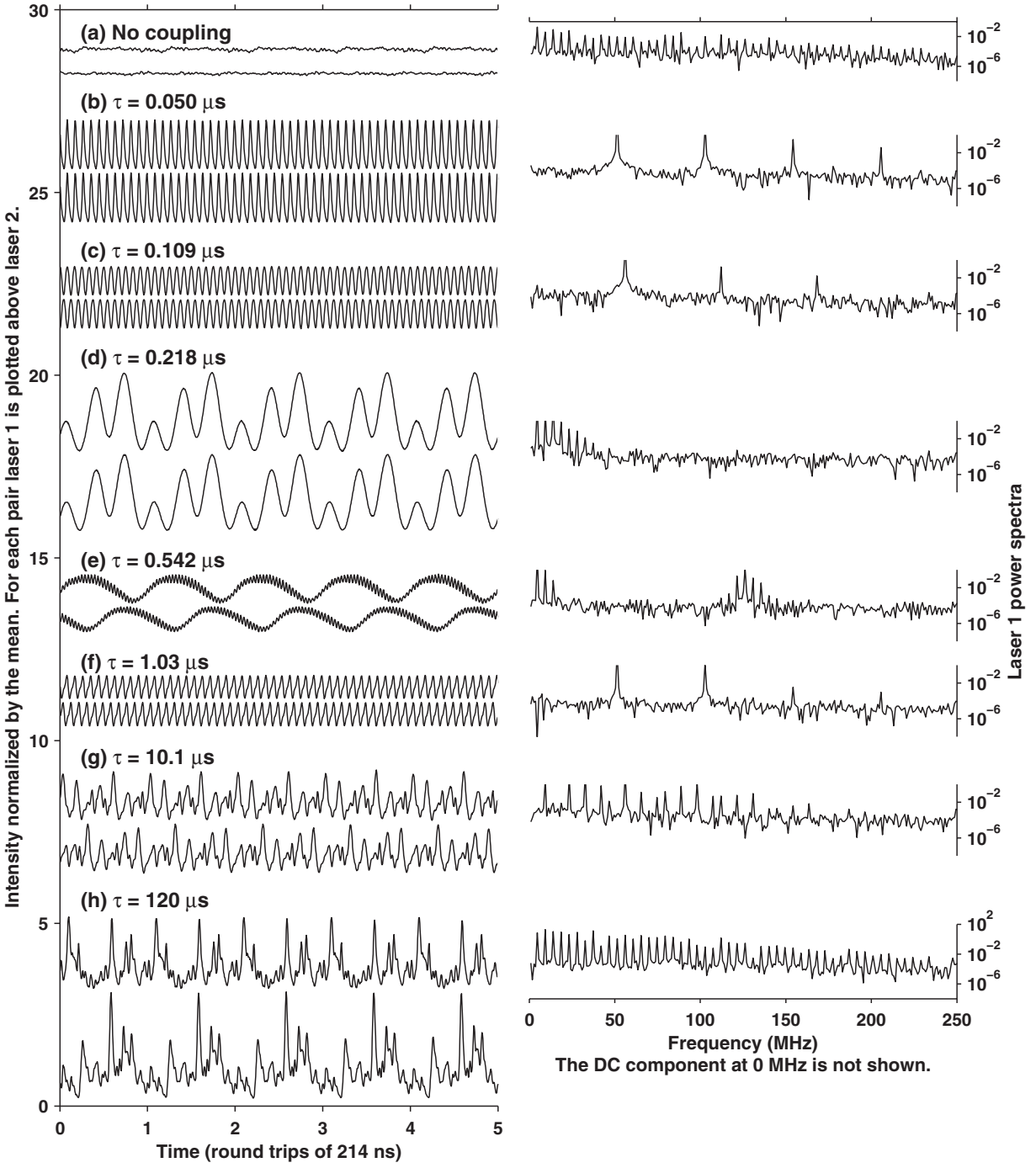

FIG. 11. Laser output intensities over five round trips where the round-trip time is 214 ns. Each time series is normalized to its mean. The plots are offset for clarity. For each pair of time series, laser 1 is offset above laser 2. (a) is for the uncoupled lasers. (b)–(i) are for the lasers coupled together with the time delay, τ, given. The right-hand column has power spectra of the five round trips shown for each time series of laser 1. The DC component at 0 Hz has been omitted to better show the detail of the spectra.

taken: One set with laser 1 setup for the feedback experiment and another set for laser 1 setup for the mutually coupled experiment. This was done to compare the mutually coupled results with the uncoupled laser operating under identical conditions. Primary differences between the two cases include different pump strengths and different tuning of the optical cavity with the polarization controllers. These were changed to match the power in the rings and the lasing wavelengths of the two lasers. The coupled lasers have larger fluctuations except at long delays when all three data sets are comparable. The ratio increases with increasing delay for the coupled lasers except when the delay time is 4 ns more than the round-trip time. The fluctuations are the largest for this delay. Without coupling, the system is constrained to repeat every round trip. With coupling, it also repeats every delay time. If the times are the same, both of these demands on the dynamics are the same.

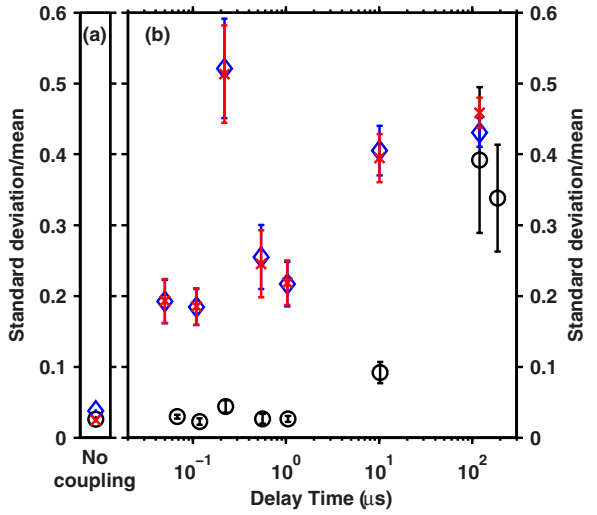

FIG. 12. (Color online) (a)Ratio of standard deviation to the mean for a single laser without feedback (○) and laser 1 (blue ◇) and laser 2 (red ×) when uncoupled. (b) Ratio of standard deviation to the mean for single laser with feedback (○) and laser 1 (blue ◇) coupled to laser 2 (red ×) with different delays. The error bars in both plots are the statistical standard error based on a sample set of 10 for the coupled lasers and five for the single laser. The single laser data (○) are reprinted from Fig. 3 for comparison.

Next we examine the complexity of the round trips for the mutually coupled lasers. The time-delay embeddings for the first round trip plotted in Fig. 11 are shown in Fig. 13. All of the plots have the same axes as the plots in (a) for the uncoupled lasers. The scale is the same as in Figs. 4(h) and 4(i), and it is easy to see how the size of the fluctuations increases even for short delays. Plots (d) and (h) are partially clipped at this scale. If the scale is reduced, Fig. 11(a) is similar to Fig. 4(a). For coupling time delays of 1 μs or less, the round-trip patterns form regular repeating structures. For longer time delays, the round-trip patterns become more complex as shown in (g) and (h).

B. Synchronization

Figures 11(b)–11(g) and 13(b)–13(g) show that the shape of the round-trip patterns for laser 1 and 2 are similar for each pair for the short section of the time series shown. This provides evidence of synchronization over a few round trips, and we want to see if it holds over the entire 1-ms time series measured. To quantify the level of synchronization we calculate the cross correlation, C_{12}, of the intensity time series of the two lasers using

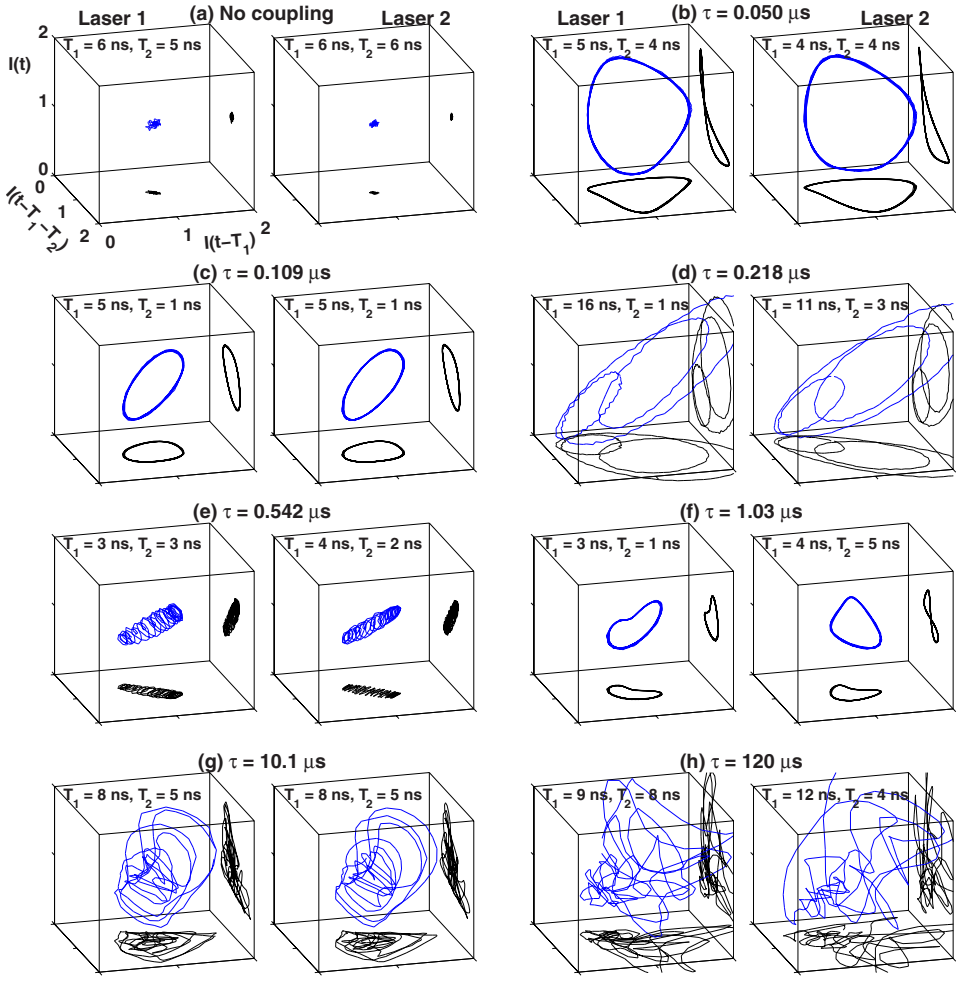

FIG. 13. (Color online) Time-delay embeddings of the first round trip shown in Fig. 11. Laser 1 is shown in the left-hand box, and laser 2 is shown in the right-hand box for each pair. Plot (a) is for the uncoupled lasers. The rest of the plots are for the mutually coupled lasers with the time delay, τ, given. The embedding delays, T_1 and T_2, are also given. The gray (blue) curve is the three-dimensional trajectory, and the black curves are 2D projections onto the bottom and right-hand sides of the plots. The data points are 1 ns apart. All plots have the same scale and are centered about 1 because each time series was normalized by its mean.

$$C_{12}(\tau_s) = \frac{1}{\sigma_1 \sigma_2} \frac{1}{J} \sum_{j=1}^{J} [I_1(t_j - \tau_s) - \langle I_1 \rangle][I_2(t_j) - \langle I_2 \rangle], \quad (9)$$

where σ_i is the standard deviation of the entire time series for laser i, J is the number of data points of overlap after sliding time series 1 by the time shift τ_s, $I_i(t)$ is the intensity of laser i at time t, and angle brackets refer to the time average of the entire time series. If $C_{12}=1$, then the time series are lag synchronized at the lag τ_s. If $C_{12}=-1$, then the signals are correlated but out of phase by one-half of a cycle. If $C_{12}=0$ then the time series are uncorrelated and not synchronized. Since previous work [20,21] found that the lasers lag synchronize with a shift $\tau_s=\tau$ when chaotic, we compute $C_{12}(\tau_s)$ over a range of τ_s that includes τ for each case.

Figure 14 shows the cross correlations of the time series plotted in Fig. 11 for different time shifts, τ_s. Plot (a) is for the uncoupled lasers, and the magnitude of the cross correlation is near zero. Plots (b)–(h) are for the lasers when they are mutually coupled. The delays are listed and also shown visually by a thick black bar. Note that the horizontal scale varies from plot to plot. Cross correlations (b), (c), and (e)–(g) are periodic with short periods compared to the coupling delays because the time series are periodic at those frequencies. Plots (b)–(h) show the leader-follower symmetry observed in the chaotic case, but the lasers are synchronized at τ only for plots (e) and (h). Plot (b) shows an isochronal case where the lasers are synchronized with no delay. Plots (c), (f), and (g) are not isochronal, but are not synchronized at τ either. For plots (b), (c), (f), and (g), $C_{12}(\tau_s) \approx -1$ indicating the lasers are approximately one-half a cycle out of phase with each other at $\tau_s=\tau$. For plot (e) $C_{12}(\tau)$ is at a maximum with respect to the low-frequency variation of $C_{12}(\tau_s)$ but is at a local minimum for the high-frequency variation. For plot (d) $\tau_r \approx \tau$, and synchronization occurs both with no delay and again at $\tau_s=\tau$. Because the round-trip patterns change so slowly, it is impossible to tell if this case has lag synchronization or isochronal synchronization. Plot (h) shows no correlation except when $\tau_s \approx \pm \tau$. The two peaks are composed of spikes occurring every τ_r that are not visible in the resolution of the plot. The long shift required for correlation explains why the plots in Figs. 11(h) and 13(h) show no evidence of synchrony over the short section of the time series shown.

The synchronization behavior for the lasers under periodic conditions is different from the behavior observed under chaotic conditions in [20]. There the synchronization was always observed to occur with a shift of $\tau_s=\pm\tau$. Here the periodic nature of the dynamics causes synchronization to occur for $\tau_s<\tau$. Plot (b) shows an isochronal case that was not observed for the chaotic data, and plot (d) is a special case as described above. We note that the authors of references [24,44] have measured stable isochronal synchronization in two mutually coupled semiconductor lasers with self-feedback when the coupling delay and the feedback delays were equal. The difference between their experiments and ours is that they have three time parameters: the short round-trip time, the mutually coupling delay, and the self-feedback delay. In our work we examine the self-feedback and the mutual coupling in separate experiments and only have two time parameters: the round-trip time and the delay corresponding to the effect we are studying. Case (h) has more complicated structures over a round trip, and its power spectrum in Fig. 15(h) shows no single strong periodicity dominating the time series. It follows the pattern for chaotic data that was observed in [20].

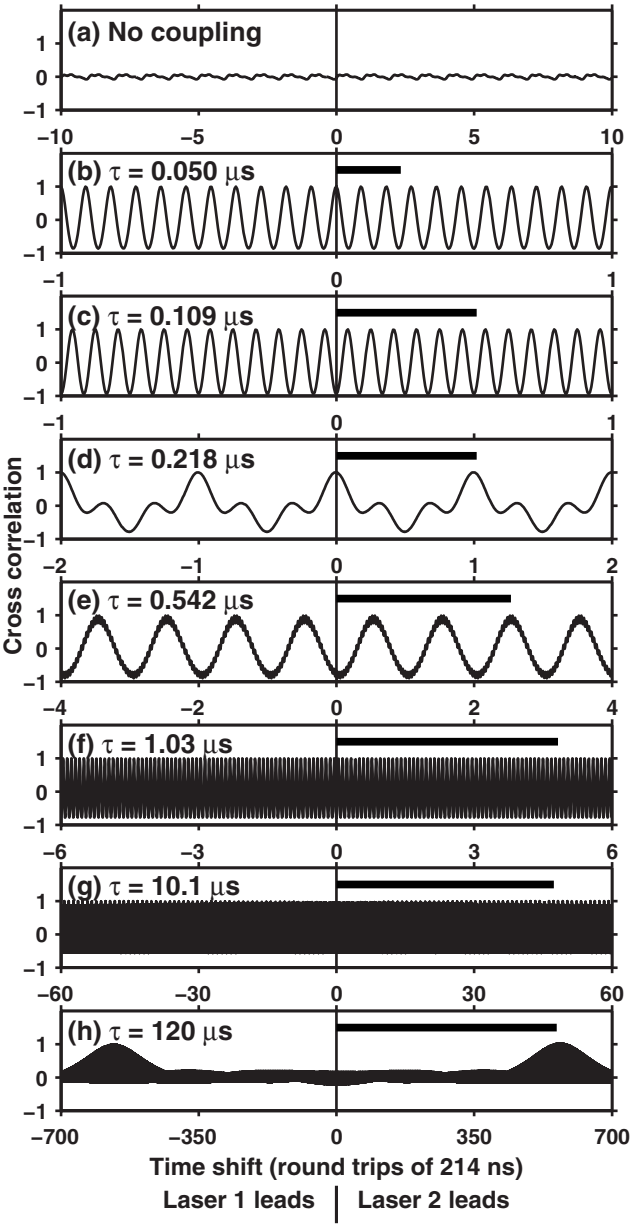

FIG. 14. Cross correlations of the entire 1 ms time series corresponding to the time-series pairs shown in Fig. 11. Plot (a) is for the uncoupled lasers. The rest of the plots are for the mutually coupled lasers with the time delay, τ, given. The thick black bars show the delay time graphically. Note that the horizontal scale of each plot changes. Negative (positive) time shifts correspond to laser 1 (2) leading.

C. Spatiotemporal representation

As in the single laser case with feedback, we want to visualize the full time series of the mutually coupled lasers.

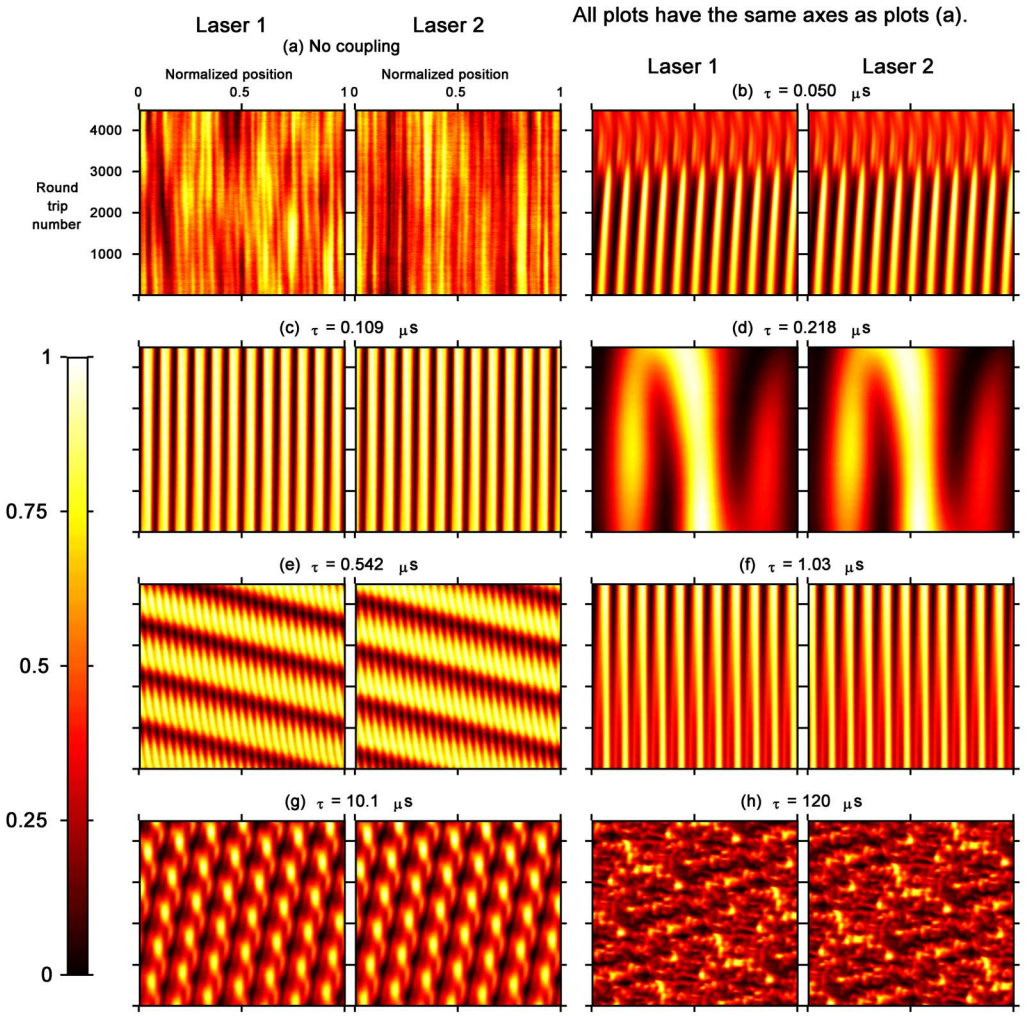

FIG. 15. (Color online) Spatiotemporal representations of the intensity dynamics of the mutually coupled lasers for (a) lasers 1 and 2 uncoupled and (b)–(h) with the coupling delays, τ, indicated. The laser intensities are rescaled from 0 to 1 for each time series with the color bar indicating the value of the normalized intensity on the plots. All plots have the same axes as plot (a).

This allows us to see the stability of the round-trip patterns and the synchronization. Figure 15 shows spatiotemporal representations for the time series containing the data in Figs. 11 and 13 which were around round trip 2430. Again, every tenth round trip is plotted up to 4500 round trips. Figures 15(b)–15(d) and 15(f) show very regular stable round-trip patterns that persist for thousands of round trips. Figure 15(e) shows a case of the superposition of low and high frequencies. Power spectra in Fig. 11 show two groups of peaks. The high-frequency peaks are harmonics of the frequency corresponding to 213.95 ns and the low-frequency peaks are harmonics that correspond to 213.78 ns. Figure 15(h) appears random at first, but structures can be seen that repeat on the order of 2 times the round-trip time. The peaks in the time series alternate from one laser to the other and it takes one delay time to move from one laser to the other. The result is a repeating pattern in the dynamics with a period of two delay times.

This repeating pattern is shown clearly in Fig. 16. These are plots of the envelope of the full 1-ms time series from which the data in Fig. 11 was extracted. The plots are labeled to match previous plots. The lasers are synchronized with a delay of τ. The repeating pattern of one laser is now 2τ. This is different than the single laser with feedback which had patterns repeating every τ as shown in Figs. 6(h) and 6(i). The bottom of Fig. 16 shows a five round-trip long section of the long data set for each laser. These two sections are offset by the time shift at which the cross correlation shown in Fig. 14(h) is a maximum. The two data sets match and show that the lasers are delay synchronized at both long and short time scales.

Figures 15 and 16 are consistent with the cross-correlation data presented in Figs. 14(g) and 14(h). Figure 15(g) shows the repetitive pattern with a time scale smaller than τ that produces the multiple spikes in C_{12}. Figures 15(h) and 16(h) show that the intensity pattern repeats with a period of τ, so C_{12} is near zero until $\tau_s = \tau$. There are spikes that occur every τ_r as well that are not visible in Fig. 14(h) due to the long time scale shown. As the time series becomes more complex the two lasers synchronize with a time shift equal to τ such as the chaotic data in [20].

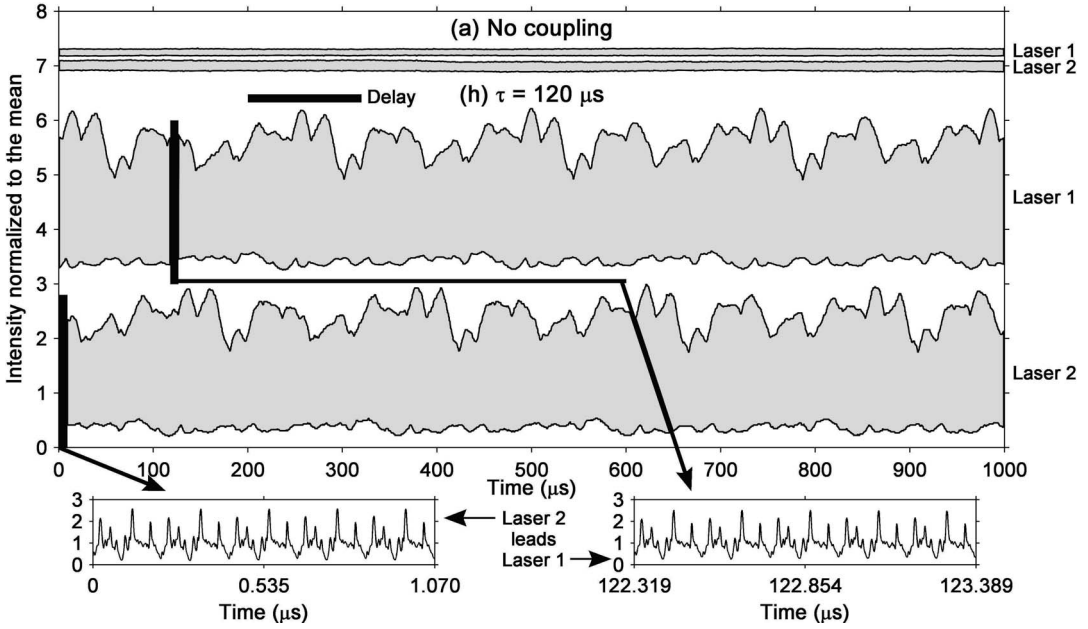

FIG. 16. Full 1-ms time series of the intensity dynamics for the lasers (a) when uncoupled and (h) when mutually coupled with $\tau = 120$ μs. The labeling corresponds to the plots in previous figures. For each pair laser 1 is offset from laser 2 for clarity. (a) is also offset from (h) for clarity. The bar on plot (h) visually shows the length of τ. The small plots on the bottom show a five round-trip portion of the long-time series from each laser. These small portions are offset by 122.319 μs which is the offset given by the maximum of the cross correlation in Fig. 14(h). The data are delay synchronized over both the round-trip and long coupling delay time scales.

D. Karhunen-Loève decomposition and spatiotemporal complexity

To quantify the complexity of the round-trip patterns we analyzed the spatiotemporal representations using KL decomposition. An example of the results for a complex time series is shown in Fig. 17 for comparison to the simpler dynamical case shown if Fig. 7. Figure 17(a) shows the spatiotemporal representation for laser 1 from Fig. 15(h). Figure 17(b) shows three KL modes where the mode numbers correspond to the eigenvalue size again. The modes are more complex here compared to those shown in Fig. 7(b) because this data set is more complex. Comparing Fig. 17(c) to Fig. 7(c) illustrates the different behavior of the expansion coefficients when the data is more complex. Here mode 10 is more significant than in the case in Fig. 7(c) and is even comparable to mode 1 for some round trips.

The normalized eigenvalue spectrum is shown in Fig. 17(d). The largest eigenvalue is an order of magnitude smaller than in the less complex case and the amplitudes fall off exponentially. The complex case requires 23 modes to reach our cutoff while the simpler case in Fig. 7 only needs three. Figures 18(a) and 18(b) show the average number of KL eigenvalues (KL modes) needed to reach the cutoff of 95% of the sum of all the eigenvalues. Figures 18(c) and 18(d) show the entropy for the same cases [43]. The data from Fig. 8 is included for comparison. In plots (a) and (c) there are two values for laser 1 for the same reasons given for Fig. 12. For the coupled lasers the number of modes needed increases for larger delays just like the single laser case. At lower delays the mutually coupled system needs fewer KL modes to capture the simple periodic dynamics. At larger delays the mutually coupled system needs more KL modes than the single laser with feedback to represent the variety of round-trip patterns produced. The entropy calculations for the mutually coupled case were previously presented in Ref. [43] and are shown here for comparison with the first method. They show similar results with a decrease in complexity for short delays and an increase in complexity for the longest delays.

One striking difference is the complexity of laser 2 in plots (a) and (c) for the uncoupled case. Counting the KL eigenvalues rates the complexity of laser 2 higher than the longest delay case and much higher than laser 1 uncoupled. The entropy of the two uncoupled lasers is similar which is expected since the spatiotemporal representations are similar. The reason for the discrepancy is revealed by examining the eigenvalue spectra of two typical cases. Figure 19 shows the 25 largest eigenvalues and the cumulative sum of the eigenvalues for the KL decomposition of the spatiotemporal representations shown in Fig. 15(a). S for laser 1 reaches the 95% cutoff before the decay rate of the eigenvalues flattens. For laser 2 the knee is rounded before S crosses the cutoff and it takes many more eigenvalues to reach it. Thus the arbitrary cutoff has a significant impact on the final value of D_{KL}. H provides a better measure of complexity for our lasers because we do not need to set a parameter arbitrarily and it gives similar values for similar spatiotemporal representations and eigenvalue spectra [compare Fig. 15(a) and Fig. 19 with Figs. 17(a) and 17(d)].

E. Optical spectra

The optical spectra of the lasers is presented in Fig. 20. Each peak is a spectral envelope of the wavelengths mea-

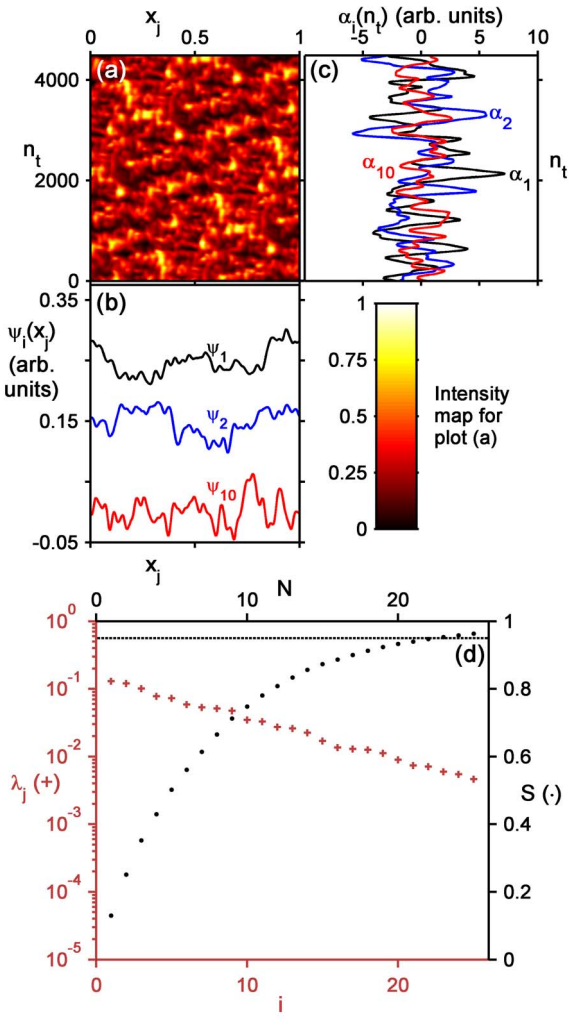

FIG. 17. (Color online) KL decomposition for τ=187 μs. (a) Spatiotemporal representation of the intensity dynamics of laser 1 from Fig. 15(h). (b) KL modes associated with the largest two eigenvalues and the tenth largest eigenvalues. Modes 1 and 2 are offset for clarity. (c) Expansion coefficients for the KL modes in (b). No single mode dominates for long periods of time. (d) The first 25 normalized eigenvalues are plotted on the left-hand axis with gray +'s (red +'s) and the cumulative sum of the eigenvalues is plotted with black dots on the right-hand axis. The dotted line shows the cutoff S=0.95. Compare with Fig. 7.

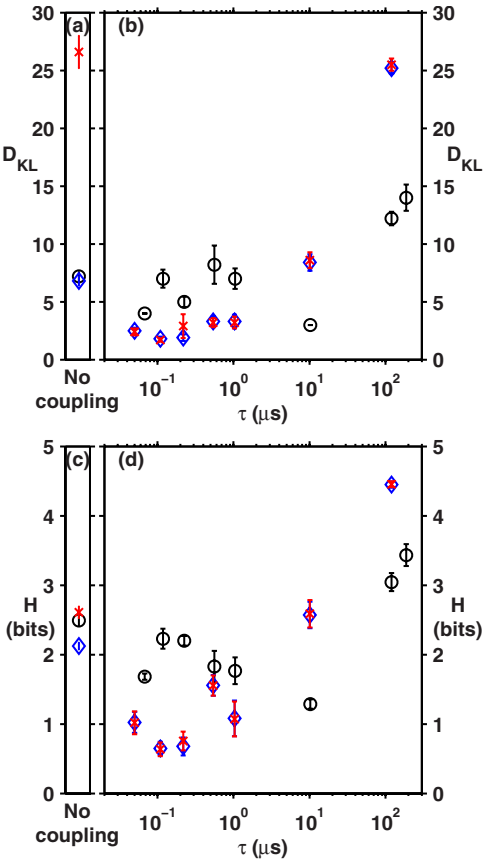

FIG. 18. (Color online) (a) Number of KL modes needed to reconstruct the spatiotemporal plot to 95% accuracy for a laser without feedback (○) and laser 1 (blue ◇) and laser 2 (red ×) when uncoupled. (b) Number of KL modes needed for 95% accurate reconstruction of the spatiotemporal plot for single laser with feedback (○) and laser 1 (blue ◇) coupled to laser 2 (red ×) with different delays. (c) Entropy for a laser without feedback (○) and laser 1 (blue ◇) and laser 2 (red ×) when uncoupled. (d) Entropy for single laser with feedback (○) and laser 1 (blue ◇) coupled to laser 2 (red ×) with different delays. The error bars in all plots are the statistical standard error based on a sample set of 10 for the coupled lasers and five for the single laser. The single laser data (black circles) are shown from Fig. 8 for comparison. The coupled laser data in (d) was presented in Ref. [43].

sured over the scan time of the OSA. The figure shows that the lasing wavelengths can shift when the lasers are coupled. For Figs. 20(c) and 20(g)–20(i) the spectra is confined to a single peak which we can compare to the uncoupled laser spectra. The height of the peaks increases by 4 times or more. This indicates an increase in the coherence of the optical fields. The increase is partially due to the reduction in width of the spectral peak which pulls more power into the central wavelengths raising the peak intensity. When the lasers are coupled the full width at half-maximum decreases from 0.2 nm to 0.1 nm. This could be due to the restriction imposed on the conditions required for lasing in the two cavities. Each cavity is tuned to operate at a certain wavelength by adjusting the polarization controllers in the cavity. Since the fiber is birefringent the light must have certain polarization states to experience high gain. When coupled to the other laser, only modes with polarization states that satisfy both laser cavities will be amplified. This limits the range of wavelengths over which the light will experience gain and hence limits the range of lasing wavelengths.

V. DISCUSSION AND CONCLUSIONS

The effect of a low level of time-delayed injected light on an EDFRL through an extra feedback loop or from mutual coupling to another EDFRL depends on the time delay. One effect observed in both experiments was the increase in the size of the fluctuations about the mean with increasing τ. For the single laser case the fluctuation size did not increase significantly until τ exceeded 10 μs. For the mutually coupled lasers the fluctuation size was significantly larger at short τ

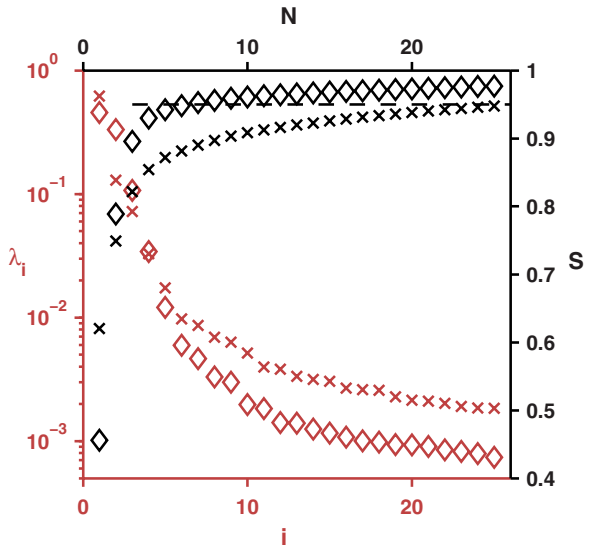

FIG. 19. (Color online) KL eigenvalue spectra and cumulative sum of the eigenvalues for laser 1 (◇) and laser 2 (×) uncoupled. The first 25 normalized eigenvalues are plotted on the left-hand axis in gray (red) and the cumulative sum of the eigenvalues is plotted in black on the right-hand axis. The dotted line shows the cutoff $S=0.95$.

than the single laser case. For longer delays the fluctuation size increased and became comparable to the single laser case at the longest delays considered. There was a significant spike in fluctuations at the resonant delay condition ($\tau=\tau_r$). The cause of the increase in fluctuation size with long delay is an open question.

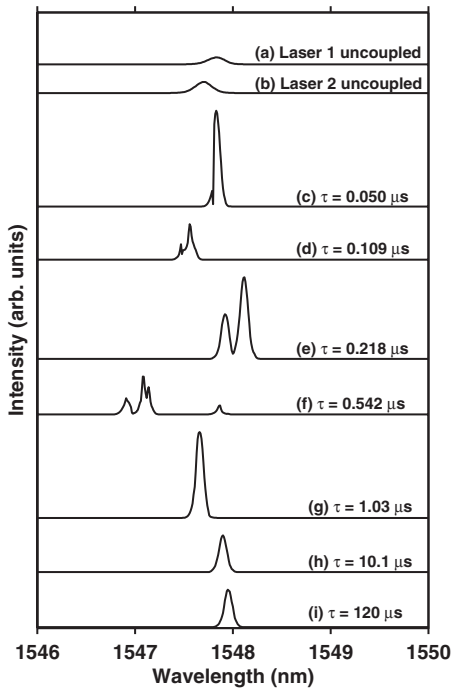

FIG. 20. Optical spectra of the lasers. (a) and (b) are for the uncoupled lasers. (c)–(h) are the sum of the light from both lasers coupled with a delay, τ, as listed.

The complexity of the dynamics also changed with different delays. For a single laser with a feedback delay comparable to τ_r, the EDFRL has periodic dynamics with periods shorter than τ_r. For τ much longer than τ_r, the dynamics repeat with periods of τ and τ_r, and the intracavity dynamics become more complex. Compared to the laser without feedback, the overall complexity as described by both the number of KL modes, D_{KL}, and the Shannon entropy, H, is comparable for small τ, decreases to a minimum at $\tau=10$ μs, and then increases for large τ. The complexity of the dynamics of two mutually coupled EDFRLs is similar to the single EDFRL with feedback. Both D_{KL} and H show a marked decrease in the complexity for short τ as compared to the uncoupled lasers and the single laser with short τ feedback. It is surprising that coupling the two lasers together could simplify their dynamics. For long τ both measures rated the dynamics more complex than the uncoupled lasers and the single laser with long τ feedback. For long τ the round-trip patterns repeat, but now the long time-scale repetition is 2τ instead of τ.

The behavior of the $\tau=10$ μs point for the single laser with feedback highlights one of the characteristics of the KL decomposition method as applied to our data. Figures 2(g) and 4(g) show that the round-trip patterns for this case are complex, yet both D_{KL} and H rated the overall complexity of the dynamics as very low. This is because even though only a few KL modes are needed to reproduce the data there are no constraints on how complicated an individual KL mode can be. If we had used Fourier modes it would have taken many more modes to represent the data. Figure 7(b) shows that the KL modes are complex in this case, while Fig. 7(c) shows that the expansion coefficients for the first two modes are large. Thus the complexity measures we use from the KL decomposition describe the overall spatiotemporal complexity of the data and do not quantify how complex the individual KL modes might be. Since the KL modes have a "length" of τ_r, these measures do not measure the complexity within a round trip.

The EDFRLs also synchronize with each other. Usually the synchronization occurs with a time shift that depends on the fast periodicity of the dynamics, but in two cases it occurs with no shift. As the dynamics become more complex for long delays, the lasers synchronize with a shift corresponding to $\pm\tau$ in agreement with previous results for chaotic data.

The spectrum of the coupled lasers collapses to roughly one-half of the width of the uncoupled lasers' spectra. This collapse of available modes does not occur in the single EDFRL with a feedback loop. As described above, in the mutually coupled case there are two laser cavities that define two independent sets of constraints on the light. Only cavity modes that satisfy the two sets of constraints will experience gain and survive. This reduction in available modes is correlated with a reduction in the complexity of the dynamics. The ability to simplify the complex dynamics of an oscillator by applying small amounts of feedback with short delays or coupling oscillators together with short delays can help organize unwanted complex behavior.

The observations in this paper allow us to gain some insight into the coherence time. From the measured spectra of

the fiber lasers in Figs. 9 and 20, we see that a typical spectral width of the uncoupled lasers is about 0.2 nm, or $\Delta_f = 17$ GHz. This width is sufficient to accommodate approximately 4000 longitudinal modes of the laser which have a spacing of 4.45 MHz (51.5 fm). If these modes were randomly phased with respect to each other, the coherence time of the light would be estimated as $\tau_c \approx 1/\Delta_f = 58$ ps. Adding a second feedback loop with variable delay time to the single laser and measuring the standard deviation of the resulting intensity fluctuations (Fig. 3) shows that a marked increase occurs for a delay time of 10 μs. This result is corroborated when the two fiber lasers are mutually coupled as well (Fig. 12). The time scale of microseconds is much longer than the estimate of τ_c above. It indicates that the effective coherence time of the fiber laser output is not determined by the measured spectral width. Instead, it is comparable to the linewidth of a single longitudinal mode. Based on estimated cavity parameters, our mode width is approximately 500 kHz which corresponds to $\tau_c = 2$ μs [45].

A way to interpret this much longer coherence time is to observe that the spatiotemporal patterns in Figs. 5 and 15 are stable over hundreds of round trips of the fiber laser cavities. This demonstrates that the phases of the individual longitudinal modes are stable relative to each other for long periods of time of the order of microseconds. If the lasers were completely mode locked one would notice a recurring ultrashort pulse on every round trip. Instead the temporal patterns in Figs. 2 and 11 show complex patterns of peaks and valleys which indicate that not all the modes are locked. These metastable repeating complex patterns could be interpreted as being due to clusters of longitudinal modes that remain in a stable phase relationship over hundreds of round trips. Figure 15, in particular, demonstrates stable phase locking of mode clusters of the mutually coupled lasers, giving rise to highly regular spatiotemporal patterns.

ACKNOWLEDGMENTS

The authors thank A. Landsman and J. Aron for helpful discussions and W. Ray for helping create some of the fiber coupling lines. We gratefully acknowledge support from the Office of Naval Research and the U.S. Air Force Center for Array Analysis. A.L.F. acknowledges support from the Air Force Institute of Technology. L.B.S. was supported by the National Research Council of the United States.

[1] M. C. Mackey and L. Glass, Science **197**, 287 (1977); R. Holz and F. W. Schneider, J. Phys. Chem. **97**, 12239 (1993); M. Kim, M. Bertram, M. Pollmann, A. von Oertzen, A. S. Mikhailov, H. H. Rotermund, and G. Ertl, Science **292**, 1357 (2001); R. Lang and K. Kobayashi, IEEE J. Quantum Electron. **16**, 347 (1980); D. V. Ramana Reddy, A. Sen, and G. L. Johnston, Phys. Rev. Lett. **85**, 3381 (2000).

[2] K. Ikeda, Opt. Commun. **30**, 257 (1979).

[3] J. D. Farmer, Physica D **4**, 366 (1982); M. J. Bünner, M. Ciofini, A. Giaquinta, R. Hegger, H. Kantz, R. Meucci, and A. Politi, Eur. Phys. J. D **10**, 165 (2000); M. J. Bünner, M. Ciofini, A. Giaquinta, R. Hegger, H. Kantz, R. Meucci, and A. Politi, *ibid.* **10**, 177 (2000).

[4] H. G. Schuster, *Complex Adaptive Systems* (Scator Verlag, Saarbrücken, Germany, 2001).

[5] G. D. VanWiggeren and R. Roy, Int. J. Bifurcation Chaos **9**, 2129 (1999).

[6] A. Argyris, D. Syvridis, L. Larger, V. Annovazzi-Lodi, P. Colet, I. Fischer, J. García-Ojalvo, C. R. Mirasso, L. Pesquera, and K. A. Shore, Nature (London) **438**, 343 (2005).

[7] G. D. VanWiggeren and R. Roy, Phys. Rev. Lett. **81**, 3547 (1998).

[8] G. D. VanWiggeren and Rajarshi Roy, Science **279**, 1198 (1998).

[9] J. García-Ojalvo and R. Roy, Phys. Rev. Lett. **86**, 5204 (2001).

[10] Q. L. Williams and R. Roy, Opt. Lett. **21**, 1478 (1996).

[11] Q. L. Williams, J. García-Ojalvo, and R. Roy, Phys. Rev. A **55**, 2376 (1997).

[12] G. P. Agrawal and N. K. Dutta, *Semiconductor Lasers* (Van Nostrand Reinhold, New York, 1993).

[13] E. Desurvire, in *Rare-Earth-Doped Fiber Lasers and Amplifiers*, 2nd ed., edited by M. J. F. Digonnet (Marcel Dekker, New York, 2001).

[14] A. E. Siegman, *Lasers* (University Science Books, Sausalito, CA, 1986).

[15] C. O. Weiss and R. Vilaseca, *Dynamics of Lasers* (VCH, New York, 1991).

[16] J. García-Ojalvo and R. Roy, Phys. Lett. A **229**, 362 (1997).

[17] L. Luo, T. J. Lee, and P. L. Chu, J. Opt. Soc. Am. B **15**, 972 (1998).

[18] L. Luo, P. L. Chu, T. Whitbread, and R. F. Peng, Opt. Commun. **176**, 213 (2000).

[19] S. Kim, B. Lee, and D. H. Kim, IEEE Photon. Technol. Lett. **13**, 290 (2001).

[20] E. A. Rogers-Dakin, J. García-Ojalvo, D. J. DeShazer, and R. Roy, Phys. Rev. E **73**, 045201(R) (2006).

[21] L. B. Shaw, I. B. Schwartz, E. A. Rogers, and R. Roy, Chaos **16**, 015111 (2006).

[22] F. Zhang and P. L. Chu, J. Lightwave Technol. **21**, 3334 (2003).

[23] T. Heil, I. Fischer, W. Elsasser, J. Mulet, and C. R. Mirasso, Phys. Rev. Lett. **86**, 795 (2001); J. K. White, M. Matus, and J. V. Moloney, Phys. Rev. E **65**, 036229 (2002); C. Masoller, Phys. Rev. Lett. **86**, 2782 (2001); L. Wu and S. Q. Zhu, Phys. Lett. A **315**, 101 (2003); J. Mulet, C. Mirasso, T. Heil, and I. Fischer, J. Opt. B: Quantum Semiclassical Opt. **6**, 97 (2004).

[24] E. Klein, N. Gross, M. Rosenbluh, W. Kinzel, L. Khaykovich, and I. Kanter, Phys. Rev. E **73**, 066214 (2006).

[25] F. Zhang, P. L. Chu, R. Lai, and G. R. Chen, IEEE Photon. Technol. Lett. **17**, 549 (2005).

[26] H. Kantz and T. Schreiber, *Nonlinear Time Series Analysis*, 2nd ed. (Cambridge University Press, Cambridge, England, 2004).

[27] H. D. I. Abarbanel, *Analysis of Observed Chaotic Data*

(Springer, New York, 1996).
[28] F. T. Arecchi, G. Giacomelli, A. Lapucci, and R. Meucci, Phys. Rev. A **45**, R4225 (1992).
[29] G. Giacomelli and A. Politi, Phys. Rev. Lett. **76**, 2686 (1996).
[30] U. Frisch, *Turbulence: The Legacy of A. N. Kolmogorov* (Cambridge University Press, Cambridge, England, 1995).
[31] M. Kirby, *Geometric Data Analysis* (Wiley, New York, 2001).
[32] J. C. Sprott, *Chaos and Time Series Analysis* (Oxford University Press, Oxford, England, 2003), p. 260.
[33] O. Hess and E. Schöll, Phys. Rev. A **50**, 787 (1994); O. Hess, Chaos, Solitons Fractals **4**, 1597 (1994);; T. Burkhard, M. O. Ziegler, I. Fischer, and W. Elsäßer, *ibid.* **10**, 845 (1999).
[34] S. Watanabe, *Transactions of the Fourth Prague Conference on Information Theory, Statistical Decision Functions and Random Processes, 1965* (Academia, Prague, 1967), pp. 635–660.
[35] T. M. Cover and J. A. Thomas, *Elements of Information Theory*, 2nd ed. (Wiley, New York, 2006).
[36] A. M. Fraser and H. L. Swinney, Phys. Rev. A **33**, 1134 (1986).
[37] L. Grassberger, T. Schreiber, and C. Schaffrath, Int. J. Bifurcat. Chaos **1**, 521 (1991).
[38] E. A. Rogers, Ph.D. dissertation, University of Maryland, 2005.
[39] I. Triandaf and I. B. Schwartz, Phys. Rev. E **56**, 204 (1997).
[40] L. Sirovich, Q. Appl. Math. **45**, 561 (1987).
[41] K. Fukunaga and D. R. Olsen, IEEE Trans. Comput. **C-20**, 176 (1971).
[42] S. M. Zoldi and H. S. Greenside, Phys. Rev. Lett. **78**, 1687 (1997).
[43] A. L. Franz, R. Roy, L. B. Shaw, and I. B. Schwartz, Phys. Rev. Lett. **99**, 053905 (2007).
[44] M. Rosenbluh, Y. Aviad, E. Cohen, L. Khaykovich, W. Kinzel, E. Kopelowitz, P. Yoskovits, and I. Kanter, Phys. Rev. E **76**, 046207 (2007).
[45] See Chap. 11 of Ref. [14] for how to calculate the mode spacing and linewidth of a cavity mode.